

# Interplay between Liquid Crystalline and Isotropic Gels in Self-Assembled Neurofilament Networks

Jayna B. Jones and Cyrus R. Safinya

Materials Department, Physics Department, and Molecular, Cellular, and Developmental Biology Department, University of California, Santa Barbara, California 93106

**ABSTRACT** Neurofilaments (NFs) are a major constituent of nerve cell axons that assemble from three subunit proteins of low (NF-L), medium (NF-M), and high (NF-H) molecular weight into a 10 nm diameter rod with radiating sidearms to form a bottle-brush-like structure. Here, we reassemble NFs *in vitro* from varying weight ratios of the subunit proteins, purified from bovine spinal cord, to form homopolymers of NF-L or filaments composed of NF-L and NF-M (NF-LM), NF-L and NF-H (NF-LH), or all three subunits (NF-LMH). At high protein concentrations, NFs align to form a nematic liquid crystalline gel with a well-defined spacing determined with synchrotron small angle x-ray scattering. Near physiological conditions (86 mM monovalent salt and pH 6.8), NF-LM networks with a high NF-M grafting density favor nematic ordering whereas filaments composed of NF-LH transition to an isotropic gel at low protein concentrations as a function of increasing mole fraction of NF-H subunits. The interfilament distance decreases with NF-M grafting density, opposite the trend seen with NF-LH networks. This suggests a competition between the more attractive NF-M sidearms, forming a compact aligned nematic gel, and the repulsive NF-H sidearms, favoring a more expansive isotropic gel, at 86 mM monovalent salt. These interactions are highly salt dependent and the nematic gel phase is stabilized with increasing monovalent salt.

## INTRODUCTION

Neurofilaments (NFs) are cytoskeletal proteins that belong to a class of structural proteins called intermediate filaments. NFs are particularly plentiful in large myelinated axons where they form a spacious network that aids in axonal transport and provides a structural scaffold within these long projections. In mature neurons of most vertebrates, NFs are heteropolymers made up of three subunit proteins of low (NF-L), medium (NF-M), and high (NF-H) molecular weights (Fig. 1 *a*). The basic structure of the subunits is similar, each having an unstructured N-terminus head domain, an  $\alpha$ -helical rod domain, and an unstructured C-terminus tail or sidearm. The subunits differ mainly in the length of the sidearms: NF-L having a short, 158-residue projection whereas NF-M and NF-H have longer 514 and 613 residue tails, respectively. When assembled into a mature filament, the N-terminal rod domain of the NF subunits forms semiflexible 10 nm diameter cylinders, with the C-terminus subunit tails radiating from the core forming a bottle-brush-like structure (Fig. 1 *b*) (1,2). NF-L subunits are unique in that they can homopolymerize whereas NF-M and NF-H must dimerize with NF-L to assemble into a filament (3). A series of assembly steps follows that include dimer association into antiparallel tetramers that form 4–5 nm diameter protofibrils, but the exact arrangement of these components within a mature filament is not well understood (4). Most likely, the organization accommodates the long NF-M and NF-H tails by arranging them on the outside of the

filament where they regulate interactions with other proteins including neighboring NFs, microtubules, and actin to form the neuronal cytoskeleton.

*In vivo*, NFs are known to associate into a network of filaments running parallel to the axon (5), forming a space-filling structure around microtubules. Although the mechanism involved in network formation is still unknown, it is presumed that the radiating sidearms play a key role in mediating interfilament spacing. Several modes of NF interactions have been proposed that span from specific sidearm attractions to a completely repulsive system that leads to a large fixed interfilament spacing. Rheological studies have found increased resistance to mechanical deformation that was attributed to cross-bridge formation (6) and is supported by electron microscopy images that show frequent links between sidearms (5,7). Another theory suggests that purely repulsive interactions in the form of a polymer brush entropic exclusion model will lead to a filament spacing comparable to that seen in axons (8). This is supported by atomic force microscope experiments showing that long-range repulsive forces exclude small particles from a 50–100 nm area around the filament core (9).

NF sidearms are polyampholytes, having both positively and negatively charged amino acids. The charge varies over the length of the subunits and is estimated in Fig. 2 for a pH of 6.8, summed locally over 10 amino acids (sequences from expasy.org protein database). The NF-L homopolymer is slightly positive near the rod-forming body domain and becomes anionic toward the protruding C-terminal end. The other subunits are similar to NF-L but they have an additional distal extremity with a distinctly different linear charge distribution for NF-M compared to NF-H. In the absence of

Submitted December 11, 2007, and accepted for publication February 14, 2008.

Address reprint requests to Cyrus R. Safinya, E-mail: safinya@mrl.ucsb.edu.

Editor: Jill Trewhealla.

© 2008 by the Biophysical Society  
0006-3495/08/07/823/13 \$2.00

doi: 10.1529/biophysj.107.127415

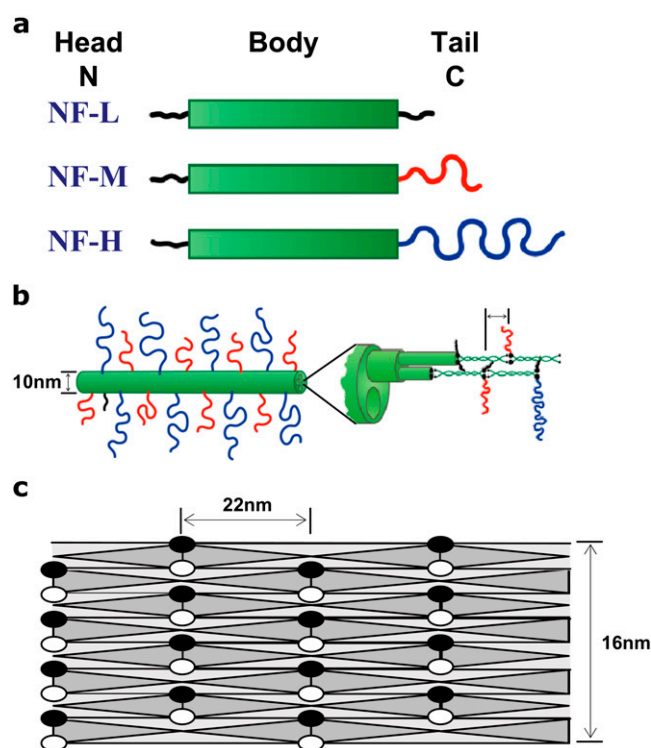


**FIGURE 1** Cartoon showing how the three subunit proteins, NF-L, NF-M, and NF-H (a) form dimers that associate into a mature filament with radiating sidearms (b, redrawn from Fuchs and Cleveland (4) and modified to show the different NF subunits). The dimers are half staggered and antiparallel in orientation, resulting in a 22 nm spacing between protruding tails along the length of the filaments. NF-L is the only subunit that can homopolymerize, whereas NF-M and NF-H can only form a dimer with NF-L. In a fully saturated filament (1:1 ratio of long tailed subunits, NF-M and/or NF-H, to NF-L) the dimers are arranged into a mature filament as shown in the schematic (c; x, y axis is not to scale), which represents one side of a filament composed of 32 total subunits or 16 per side. Each “X” is one dimer and the solid ovals symbolize the sidearm protrusions of either NF-M or NF-H; the open ovals signify NF-L tails.

phosphorylation, NF-M has several blocks of locally cationic residues, one being at the tip of the tail, but the net charge is anionic (Table 1, NF-M no phosphorylation). NF-H, on the other hand, contains nearly evenly distributed alternating

positive and negative charges resulting in a net neutral sidearm (Table 1, NF-H no phosphorylation).

The net charge and linear charge distribution of the subunit sidearms is highly dependent on the degree of phosphorylation. NF-M and NF-H, in particular, have many serine residues that can be phosphorylated, adding an additional  $-1.8$  charge at pH 6.8, for each modified residue (10). The regions along the subunits having many phosphorylatable groups are marked in Fig. 2. For NF-M and NF-H subunits, the average phosphorylation state has been determined using tandem mass spectroscopy and is also plotted in Fig. 2 (NF-M, average phosphorylation) to show how dramatically the local charge can vary with posttranslational modification (11). Bovine NF-M sidearms, with average phosphorylation, contain a large anionic central domain with smaller cationic domains near the body and tip and an overall charge of  $-99e$  (12). The average phosphorylation of mouse NF-H has a total sidearm charge of  $-92e$  that is distributed with half the tail near the body being strongly anionic with the remaining C-terminus containing alternating cationic/anionic domains. Gel electrophoresis has shown that bovine NF-H is more negatively charged than NF-M (13) although site specific phosphorylation studies have yet to be done. Both NF-M and NF-H tails are highly negatively charged after phosphorylation, resulting in a polyelectrolyte brush when incorporated into a filament. It follows that forces that dictate polyelectrolyte properties, such as brush layer thickness resulting from an interplay between chain elastic energy and electrostatic forces, will be relevant in this system as well.

The properties of polyelectrolytes in solution (14) and under confinement, including end grafting to different geometries, most commonly planar, spherical, and cylindrical substrates (15,16), have been extensively studied. Significant strides have also been made toward understanding polyampholytes, due to their relation to understanding protein interactions, but to a lesser extent than polyelectrolyte interactions (17). In most cases, polyion studies have been based on a model system with a homogeneous linear charge density. NF interactions are more complicated with a varying distribution of ionizable groups along the length of the sidearm as well as phosphorylatable groups. Slight changes in pH control the local and overall charge on the sidearms, producing a polyampholyte at low pH and an unsaturated polyelectrolyte at higher pH. Additionally, the sidearm charge distribution among the three subunits is different, suggesting that subunit composition of the filaments will alter interfibrillar interactions.

The arrangement of the subunits within a filament is an important parameter because it reveals the distribution of the long protruding sidearms along the core which, for one, is critical for determining nearest neighbor interactions. If the tetramers are arranged in a half-staggered fashion, which is the most widely accepted organization, the sidearms can be attached no closer than 22 nm apart along the length of the filament (half of the length of the  $\sim 45$  nm coiled-coil dimer).

**TABLE 1** Comparison of the amino acid length, fraction of charged amino acids (AA), fraction of the charged amino acids that are negatively charged, the net charge, and the average charge per amino acid along the sidearms of the three NF subunit proteins

Sidearm	Total length (AA)	Fraction charged AA	Fraction AA negatively charged	Net charge (e)	Average charge (e)/AA
NF-L (bovine, no phos)	158	0.45	0.77	-39.6	-0.25
NF-L (bovine, ave phos)	158	0.46	0.78	-41.2	-0.26
NF-M (bovine, no phos)	514	0.47	0.59	-47.4	-0.09
NF-M (bovine, ave phos)	514	0.52	0.63	-99.4	-0.18
NF-H (mouse, no phos)	679	0.42	0.49	-2.6	0.02
NF-H (mouse, ave phos)	679	0.49	0.58	-91.8	-0.14

Values are given for no phosphorylation and average phosphorylation (11,12).

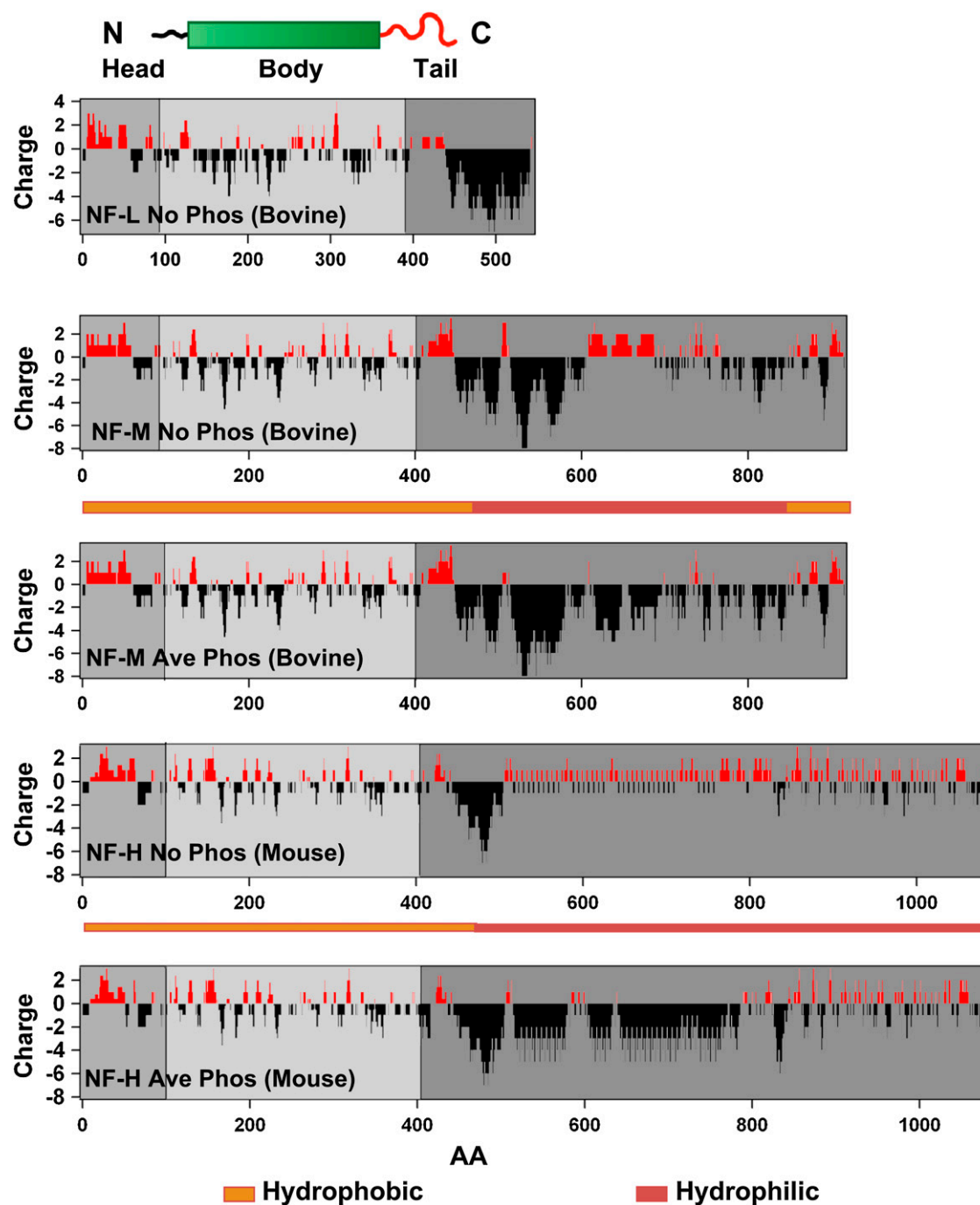


**FIGURE 2** Estimate of the charge distribution of the NF subunits with a rolling sum over 10 amino acids (18). The head, body, and tail domains are represented by the blocked regions along the plot from N-terminus to C-terminus, respectively. The charge distribution was calculated by assuming the charge of a single amino acid in solution at pH 6.8. Plots for NF-L (bovine), NF-M (bovine), and NF-H (mouse) without phosphorylation show the slightly negative tail of NF-M and overall charge neutral NF-H. NF-M and NF-H are highly phosphorylated, which changes each modified amino acid from neutral to approximately a  $-1.8$  charge (sequences from expasy.org protein database). The bar between the NF-M and NF-H curves indicates the hydrophobicity of the subunits. The rolling sum over 10 amino acids of the average phosphorylation state is also plotted for NF-M (11) and NF-H, showing how dramatically the charge distribution changes with posttranslational modification. The curves show that NF subunits are polyampholytes, having both positively and negatively charged regions along the sidearm projection.

Since NF-M and NF-H must dimerize with NF-L, the maximum number of long protrusions possible is one per dimer (1:1 molar ratio of NF-L:NF-M,NF-H). NFs purified from fractions of bovine spinal cord have a subunit molar ratio of 7:3:2 for NF-L:NF-M:NF-H (1 NF-L:NF-L, 3 NF-L:NF-M, and 2 NF-L:NF-H dimers) (18). If the filaments are arranged in the manner shown in Fig. 1 *b* with half-staggered dimers and 32 subunits in cross section, then this would give an average distance between long protrusions of  $\sim 22$  nm along the length of the filament and 4–5 nm radially as depicted in Fig. 1 *c* (19,20).

This ratio is an average composition while in actuality the subunit ratio varies locally and has been correlated with changes in interfilaments spacing in vivo with filaments rich in NF-L having a smaller spacing than those coassembled with NF-M and NF-H (21). During axonal development, subunits are expressed at different stages with NF-L, then NF-M appearing during early neuron differentiation followed by NF-H at later stages of axonal maturation (22,23). In adult neurons, regional differences in NF composition exist where different subunit ratios have been observed in the cell body versus the axon (24). Furthermore, the stoichiometry is dynamic during nerve regeneration and cytoskeletal reorganization where NF-H disassembles and is later reintroduced into the filament (25). These observations prompt questions about the function of subunit ratio on filament assembly and network formation.

Breakdown of subunit composition regulation has been implicated in several neurological disorders. Over- or underexpression of NF subunits in transgenic mouse models leads to protein inclusions similar to those seen in diseases including Parkinson's, ALS, and Charcot-Marie-Tooth (26–31). A hallmark of these diseases is NF accumulations and network breakdown that block the transport of proteins and other vital molecules down the axon, eventually resulting in cell death. Although many experiments have shown the importance of subunit stoichiometry for proper function and signal conduction within neurons, systematic studies showing the effects of subunit composition on NF interactions have yet to be done.

Here, the exact molar ratio of subunits, and therefore the grafting density of sidearms, in vitro, is controlled by using subunits purified from bovine spinal cord. We create filaments composed of NF-L alone and various ratios of NF-L and NF-M (NF-LM), NF-L and NF-H (NF-LH), or all three subunits (NF-LMH). By varying the composition of subunits used in NF assembly, we find that the distinct chemical structure of NF-M and NF-H sidearms may result in dramatically different physical networks that are either aligned into nematic gels or form disordered isotropic gels. Polarized microscopy and synchrotron small angle x-ray scattering (SAXS) show that around physiological monovalent salt concentrations (86 mM and pH 6.8), networks assembled with NF-M sidearms form a nematic gel with a fixed inter-filament spacing of 48 nm that results from competing re-

pulsive and attractive forces. NFs assembled with a high weight % NF-H are dominated by repulsive forces that prevent alignment of filaments into a nematic network without an applied force. These interactions are highly salt dependent and both the nematic and isotropic gel phase can be induced in all NF networks regardless of subunit composition, suggesting that attractive interactions play a key role in stabilizing the nematic network.

## MATERIALS AND METHODS

### Crude NF purification

Crude NFs were purified from bovine spinal cord according to the procedure described by Leterrier and Eyer (32) and modified by Leterrier et al. (6). Spinal cords were homogenized in an equal weight of buffer A (0.1M MES, 1mM EGTA, 1mM  $MgCl_2$ , 0.02 wt % sodium azide, pH 6.8 with NaOH) then centrifuged at  $100,000 \times g$  for 1 h at 4°C. The supernatant was incubated with half the volume of glycerol for 3 h. A pellet of NFs was recovered from the glycerol solution by sedimentation for 1.5 h again at  $100,000 \times g$ . The resulting NF pellet was homogenized in buffer A and clarified by spinning through a step gradient of 0.8 M sucrose buffer (0.8 M sucrose in buffer A) layered on 1.5 M sucrose buffer (1.5 M sucrose in buffer A) for 4 h at  $300,000 \times g$ . The pellet was resuspended in 0.8 M sucrose buffer and by dropwise addition to liquid nitrogen and stored at  $-70^\circ C$  awaiting further purification.

### Subunit purification

Additional purification using ion-exchange chromatography was needed to remove any remaining contaminants and to separate the three NF subunits (33). Frozen crude NFs were quickly thawed under warm water with agitation and pelleted by centrifugation for 2 h at  $300,000 \times g$ . The pellets were homogenized in enough buffer B (0.1 M sodium phosphate and 0.1 vol % 2-mercaptoethanol in 8 M urea, pH 6.5) so that the final urea concentration remained above 6 M and incubated overnight to completely denature the filaments. The denatured filaments were applied to a DEAE-cellulose column (Sigma-Aldrich, St. Louis, MO), equilibrated with buffer B, to separate the contaminating proteins and NF-H from NF-L and NF-M. The column was rinsed thoroughly with buffer B, which eluted all NF-H and protein contaminants in the void volume. Pure NF-M was eluted with the addition of buffer B with 55 mM added NaCl. Finally, increasing the pH of buffer B, with 55 mM NaCl, to 7.0 with  $5\times$  dibasic sodium phosphate in 8 M urea eluted NF-L and any remaining NF-M. Generally, the NF-L was contaminated with a small amount of NF-M and the purity was checked with a 7.5% SDS-PAGE.

Using hydroxylapatite chromatography (Bio-Gel HT gel, Bio-Rad, Hercules, CA), the contaminants were removed from the NF-H fractions and NF-L and NF-M were recovered individually. First, fractions of NF-H with contaminants from the DEAE-cellulose column were concentrated with Centricon tubes (Millipore, Bedford, MA) and applied to an HT column equilibrated with buffer B. The contaminants remained in the void volume while NF-H eluted with 0.4 M sodium phosphate (with 0.1 vol % 2-mercaptoethanol in 8 M urea, pH 7.0). The column was thoroughly rinsed with the 0.4M sodium phosphate then equilibrated with buffer B. Fractions from the DEAE-cellulose column that contained NF-L and NF-M subunits were concentrated (Centricon tubes) and the buffer was exchanged with buffer B to remove the NaCl and bring the pH down to 6.5. The filaments were then applied to the HT column and a series of elution buffers, 0.13 M, 0.15 M, 0.17 M, and 0.2 M sodium phosphate with 0.1 vol % 2-mercaptoethanol in 8 M urea, pH 7.0 were added. NF-L typically eluted in the 0.15 M sodium phosphate buffer with any remaining protein rinsing out at 0.17 M sodium

phosphate. The NF-M subunits eluted with the high sodium phosphate concentration. Purity was checked with SDS-PAGE and fractions were combined and concentrated to  $\sim 4$  mg/mL.

### Determination of maximum sidearm grafting density

NFs were assembled by dialysis overnight against buffer A to remove urea and 2-mercaptoethanol, with an increasing ratio of NF-M:NF-L or NF-H:NF-L. Postdialysis protein concentration was determined using a Bradford assay and the NFs, at a concentration  $>2$  mg/mL, were centrifuged for 1 h at  $100,000 \times g$ . The supernatant was immediately removed from the pellet. The protein concentration of the supernatant was checked using a Bradford assay and the composition was determined with SDS-PAGE and gel analysis with ImageJ (National Institutes of Health). Subtracting the amount of each subunit protein remaining in the supernatant from the initial protein before sedimentation gives the composition of the pellet. Any protein remaining in the supernatant was considered unassembled NFs.

### NF dilution and monovalent counterion experiments

NFs were assembled at various subunit ratios by dialysis against buffer A. For monovalent salt samples, an equal volume of KCl solution was added to the NFs making the final buffer concentration half that of buffer A. This gives a total monovalent salt concentration equal to 43 mM (from buffer contribution) plus the concentration of additional added KCl. NFs at a concentration  $>2$  mg/mL were pelleted by sedimentation for 1 h at  $100,000 \times g$ . The supernatant was immediately removed and the pellets were applied to 1.5 mm glass capillaries and diluted with supernatant to the desired volume fraction and characterized with polarized microscopy and SAXS.

### Polarized optical microscopy

Sedimented NFs were observed in 1.5 mm glass capillaries using a Nikon (Tokyo, Japan) 282130 microscope fitted with a  $5\times$  objective. Micrographs were taken with a Nikon Coolpix 990 camera fitted with a MDC lens.

### X-ray scattering

SAXS experiments were conducted at Stanford Synchrotron Radiation Laboratory beamline 4-2. Scattering was collected using a 1.37 nm wavelength with a sample-to-detector distance of  $\sim 2.5$  m, calibrated using a silver behenate standard. Samples were exposed for 5 min and the resulting powder

diffraction patterns were acquired on a MarCCD 165 detector (Rayonix LLC, Evanston, IL). The images were integrated over  $360^\circ$  using Fit2D (34,35) software to obtain plots of intensity versus  $q$  spacing. Peak positions were extracted by subtracting a linear baseline then performing a Lorentzian fit.

## RESULTS AND DISCUSSION

### Sidearm grafting density

With the goal of determining the effect subunit composition has on interactions between filaments, it is important to characterize the polymerization when varying the subunit ratio. To accomplish this, a series of experiments were conducted that determined the composition of filaments assembled from an initial solution of unpolymerized subunits of varying ratio. NF-L subunits will assemble alone to form homopolymers whereas NF-M and NF-H subunits must dimerize with NF-L to form filaments (5). Therefore, theoretically, the maximum grafting density would be a 1:1 molar ratio between NF-L/NF-M or NF-L/NF-H. In reality, the final composition of an assembled filament will depend on the initial ratio of subunits in the assembly solution and how well the subunits associate with one another during polymerization.

The filament composition was determined for an initial solution of subunits as a function of increasing ratio of NF-M (Fig. 3 *a*) or NF-H (Fig. 3 *b*) to NF-L. The linear dependence at low weight % NF-M or NF-H subunits shows that they are still assembling into filaments at the same rate they are added to the assembly solution, indicating that saturation has not occurred. The slope of each curve gives the efficiency that NF-M or NF-H will dimerize and form a filament with NF-L. The 0.96 slope of the NF-LM curve indicates that the subunit ratio, after filament assembly, is nearly that of the initial subunit composition. NF-H has a less efficient addition rate where at an initial solution concentration of 20 wt % NF-H subunits and 80 wt % NF-L, only 80% of the NF-H subunits will incorporate into the assembled filament giving 16 wt % NF-H. The region where the curves begin to deviate from the initial slope is the maximum grafting density. Above this point, additional NF-M or NF-H subunits will not assemble into the filaments and instead remain in the supernatant after

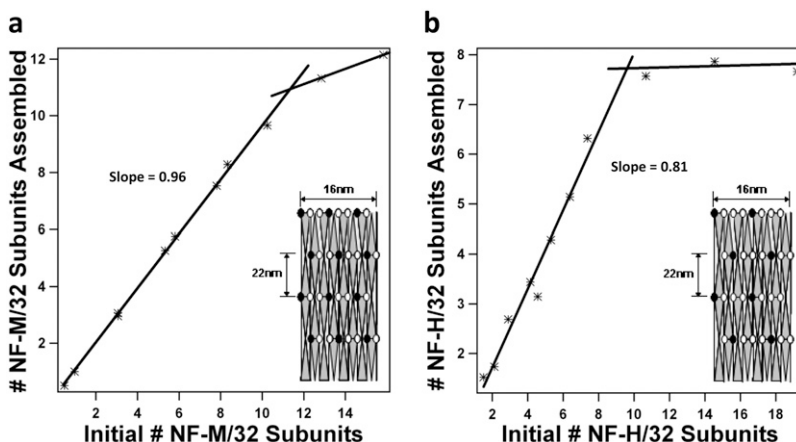


FIGURE 3 Curves showing the number of long-tailed subunits NF-M (*a*) and NF-H (*b*) that assemble (86 mM monovalent salt) with NF-L into a filament for a given initial composition before dialysis. The saturation point of NF-LM and NF-LH networks is the maximum number of NF-M or NF-H subunits that can assemble into a filament and is given by the point where the curves deviate from the initial linear slope. The maximum grafting density for NF-LM networks is 12 NF-M subunits per 32 total subunits and for NF-LH it is 8 NF-H subunits per 32 total subunits. The assembly efficiency is given by the slopes of the initial linear regions. The insets show a schematic representation of the distribution of the subunit tails for the saturation point as described in Fig. 1.



centrifugation. This occurs at  $\sim 36$  mol % (48 wt %) NF-M and 29 mol % (45 wt %) NF-H for the initial solution, which results in nearly the same filament composition for NF-M and 25 mol % (40 wt %) for NF-H. For the remainder of this article, the term sidearms will refer to the longer protruding NF-M or NF-H C-terminal tails. Consequently, the distance between tails and the grafting density refers to the packing of NF-M and NF-H subunits along the rod, and the shorter NF-L tails are disregarded in these values.

In cross section, intermediate filaments are composed of  $\sim 32$  subunits (4 protofilaments), although this can range from 24 to 40 subunits (between 3 and 5 protofilaments) (36,37). For ease of determining the distance between sidearms along the core, the grafting density data have been normalized to 32 total subunits. At the maximum grafting density, there are 12 NF-M and 8 NF-H sidearms per 32 subunits for NF-LM and NF-LH heteropolymers, respectively. Again assuming half-staggered dimer assembly, this would give a distance of  $\sim 5$  nm between NF-M sidearm projections (Fig. 3 *a*, *inset*) and 8 nm between NF-H protrusions (Fig. 3 *b*, *inset*) around the circumference of the rod and 22 nm along the length of the filament. Previous assembly studies by Hisanaga and Hirokawa have shown the formation of shorter filaments upon reassembly from urea compared to crude filament purification (38,39). Electron micrographs of our assembled subunits show filaments that are  $\sim 100$ – $200$  nm in length that associated into longer filaments at high concentrations (shown in the Supplementary Material figures, [Data S1](#)).

### Phase behavior and interfilament interactions in NF-LM and NF-LH networks

To determine the phase behavior of NF networks resulting from interfilament interactions at different subunit ratios, NFs were assembled with an increasing ratio of NF-M/NF-L or NF-H/NF-L subunits starting with homopolymers of NF-L and using the maximum sidearm grafting density as the upper limit for assembly. The phase behavior as a function of total protein concentration was mapped out with polarized optical microscopy and compiled into two component phase diagrams (Figs. 4 *a* and 5 *a*). The phase diagram for NF-M assembled with NF-L at 86 mM monovalent salt and pH 6.8 is shown in Fig. 4 *a*. At high weight % protein, the gels are one-phase nematic ( $N_G$ ). The  $N_G$  phase exhibits defect patterns between crossed polarizers similar to those of nematic phases of small anisotropic rod-shaped molecules (Fig. 4 *b*). The characteristic “thread-like” pattern is indicative of the long-range orientational order of the backbone filaments in the NF network. As the NF gels are diluted to low weight % total protein, the single phase gel swells until a dilution limit is reached, beyond which a transition to a nematic gel and isotropic sol is observed. This transition is  $\sim 1.5$  wt % total protein for NF-L homopolymer but increases with the addition of NF-M sidearms. Further dilution results in an in-

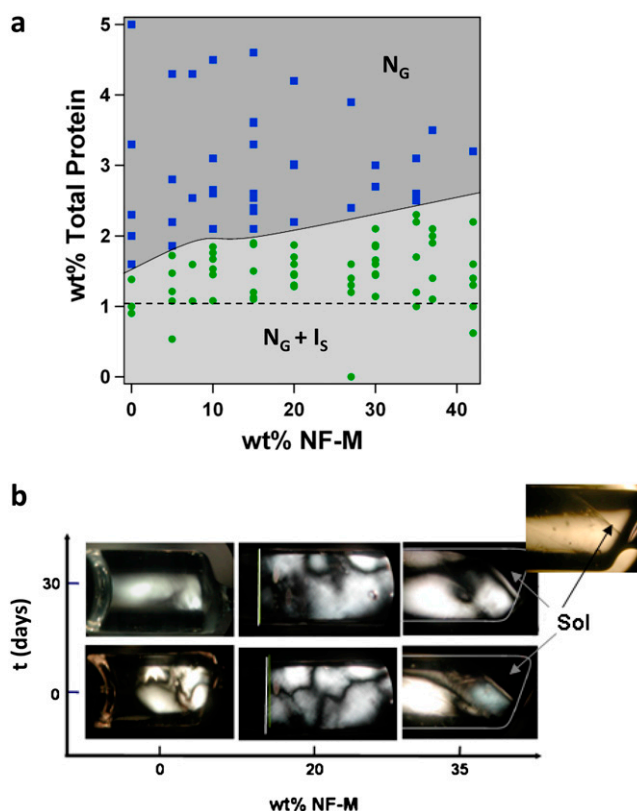


**FIGURE 4** (a) Phase diagram showing the phase behavior, as determined via polarized microscopy, of NF-LM networks composed of increasing weight % NF-M as a function of total protein concentration (NF-L + NF-M) for a monovalent salt concentration of 86 mM. At high weight % total protein, the NFs form a nematic gel ( $N_G$ ). The nematic gel is stabilized even at low weight % total protein where a two-phase nematic gel and isotropic sol ( $N_G + I_S$ ) is reached. The transition to the two-phase region occurs at a higher weight % total protein as the NF-M grafting density is increased (*solid line* is a guide for the eye). Exemplary polarized micrographs (*b*) show the behavior of NF-LM networks at  $\sim 1$  wt % total protein (samples from the *dashed line* on the phase diagram from *a*) immediately after dilution and after equilibration of 30 days. Gel swelling can be seen in both the 0 wt % NF-M (100:0, NF-L/NF-M) and 20 wt % NF-M (80:20, NF-L/NF-M) whereas no gel swelling is seen upon dilution of the 35 wt % NF-M (65:35, NF-L/NF-M) networks. Bright field image (*inset*) shows a pellet with an asymmetric interface and a clear, not milky, appearance, indicating that the network is a gel.

creased volume of isotropic sol phase with a fixed nematic gel. At the maximum grafting density analyzed, 40 wt % M (25 mol %), minimal gel swelling occurs.

The liquid crystalline and gel behavior is observed readily in polarized optical microscopy. Fig. 4 *b* shows polarized micrographs taken of the same samples, from the two-phase region (*dashed line* in Fig. 4 *a*), immediately after dilution,  $t = 0$ , and after an equilibration period of  $t = 30$  days. Swelling of the NF-L (0 wt % NF-M, micrographs at *left*, Fig. 4 *b*) homopolymer is dramatic showing distinct nematic ordering during initial dilution,  $T = 0$ , and much weaker birefringence at  $t = 30$  days. The diminishing birefringence intensity with gel swelling is an indication of a decrease in the nematic order parameter corresponding to less orientational

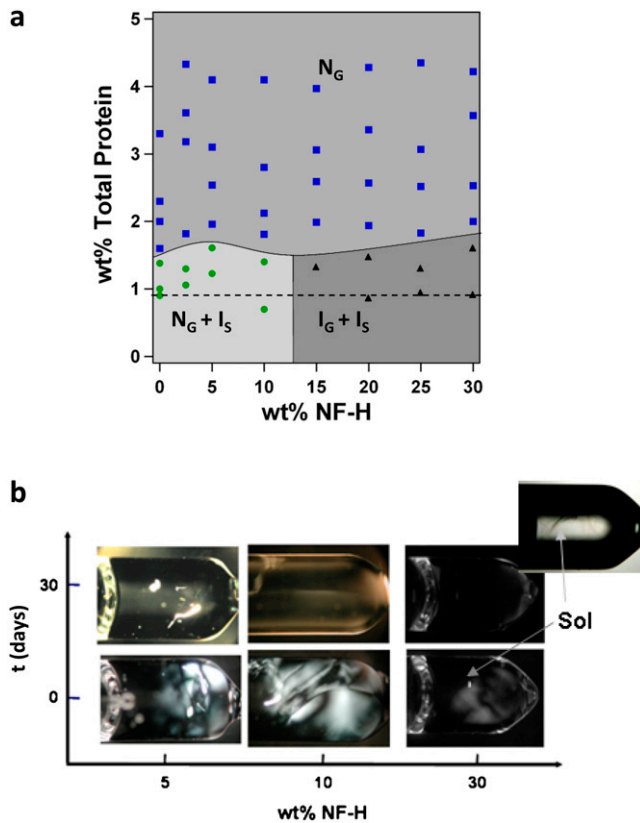


**FIGURE 5** (a) Phase diagram showing the phase behavior, as determined via polarized microscopy, of NF-LH networks composed of increasing weight % NF-H as a function of total protein concentration (NF-L + NF-H) for a monovalent salt concentration of 86 mM. At high weight % total protein, the NFs form a nematic gel ( $N_G$ ) for all compositions. For low grafting densities of NF-H (<15 wt % NF-H), the nematic phase is stabilized at low weight % protein where the system becomes two-phase ( $N_G + I_S$ ). Increasing weight % NF-H has the opposite effect of adding NF-M sidearms, resulting in a disordered isotropic gel + isotropic sol ( $I_G + I_S$ ) at low weight % total protein (solid lines are guides for the eyes). Exemplary polarized micrographs show the behavior of NF-LH (b) networks at ~1 wt % total protein (samples from the dashed line on the phase diagram from a) immediately after dilution and after equilibration of 30 days. The bright field image (inset) shows an asymmetric interface, indicating that the network is a gel.

order among filaments. At high NF-M grafting density (35 wt % NF-M, micrographs at right, Fig. 4 b), the gel remains fixed over time with no detectable swelling showing a stabilization of the nematic phase with NF-M grafting density. NFs in the nematic phase are always clear by eye and under bright field microscopy, unlike the milky appearance typical of a nematic phase, (Fig. 4 b, inset), which shows that local chain fluctuations have been suppressed by gelation (40).

A distinctly different phase behavior is seen in heteropolymers composed of NF-L and NF-H with increasing weight % NF-H (Fig. 5 a). Similar to the NF-LM gels, with low NF-H grafting densities, the resulting network is one-phase ( $N_G$ ) at high weight % total protein and two-phase nematic gel/isotropic sol ( $N_G + I_S$ ) when diluted to a lower total protein concentration. Increasing the weight % of NF-H subunits leads to a destabilization of the nematic gel at high

dilution that was not observed in the NF-LM network. For  $NF-H > 10$  wt % total protein, the NF-LH network is in the  $N_G$  phase with the filaments oriented, as indicated by the nematic liquid crystalline texture seen under polarized light, but become isotropic gels upon dilution. This transition from a nematic to an isotropic gel after dilution is shown in the optical micrographs (Fig. 5 b) where at time  $t = 0$ , immediately after the gels are diluted, the NFs have a nematic liquid crystalline texture although the birefringence is noticeably less bright than the NF-LM micrographs. This indicates that even at the highest protein concentration probed, the nematic orientational order of the networks is considerably reduced, most likely with enhanced thermal fluctuations in the NF-LH system. After equilibration for 30 days, destabilization of the nematic phase, as evident from total extinction of light, shows that the gel is no longer orientationally ordered whereas the asymmetric interface, seen under bright field optical microscopy (inset in Fig. 5 b), shows that the networks are still gel-like with elasticity resisting flow.

### SAXS reveals interfilament spacing of NF-LM and NF-LH networks

SAXS was conducted on the samples shown in the phase diagrams (Figs. 4 a and 5 a), and exemplary raw data, integrated azimuthally over a two-dimensional image of the powder diffraction pattern, is plotted against the scattering angle  $q$  (Figs. 6 a and 7 a). The scattering profiles exhibiting broad peaks arise from filament-filament interactions within the  $N_G$  network. The position of the peak ( $q_{NF}$ ) is a measure of the average center-to-center NF interfilament spacing,  $d = 2\pi/q_{NF}$  (Figs. 6 b and 7 b). Each point within the phase diagrams was probed to determine how interfilament spacing changes with filament subunit composition. The x-ray peak broadening arises from two sources. First, since x-rays couple directly to density fluctuations, there is width broadening. Second, the density and nematic director field ( $\hat{n}(\vec{r})$ ) are coupled for nematic phases composed of long semiflexible chains (such as the  $N_G$  phase). Thus thermal fluctuations of the neurofilaments within the network will also contribute to the peak broadening in addition to giving rise to enhanced SAXS around  $q = 0$  (41–43). The filament fluctuations are controlled by the elastic constants of the liquid crystal  $N_G$  phase, namely the bend (single filament stiffness constant), splay, and twist constants. Therefore, a detailed lineshape analysis of the SAXS data including the peak profile (beyond the scope of this study) should lead, in principle, to the determination of the NF stiffness (persistence length), and the twist and splay constants in the nematic gel phase. The elastic constants, in turn, result from NF-NF interactions.

Fig. 6 a shows the scattering intensity from NF-LM networks with increasing NF-M grafting density. The plots on each curve show the shift in the correlation peak to smaller  $q$  values as the networks are diluted to a lower total protein concentration with a fixed subunit composition. Typical data

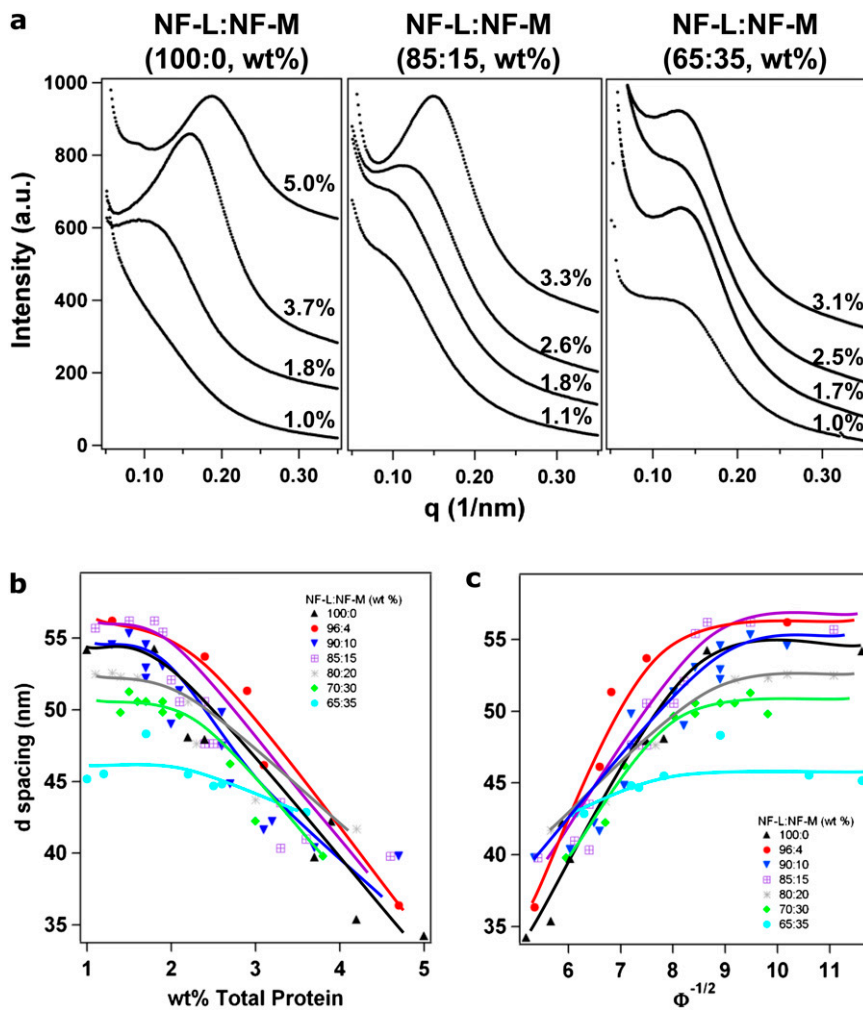


FIGURE 6 SAXS scans of dilution series of NF-LM networks (a) at 86 mM monovalent salt (shown on a log-log scale with dilution series at additional compositions in the Supplementary Material figures, [Data S1](#)). The sharp correlation peak is related to the interfilament spacing, and an inward shift of the peak position corresponds to an increase in interfilament spacing. The curves are labeled with the weight % total protein. A compilation of the center-to-center interfilament distance ( $d$  spacing) versus weight % total protein shows a decrease in spacing with increasing NF-M grafting density (b). The  $d$  spacing was found by subtracting a linear background from SAXS intensity plots and fitting the resulting first order peak to a Lorentzian curve. Plotting the  $d$  spacing versus volume fraction<sup>-1/2</sup> ( $\Phi^{-1/2}$ ) for various weight ratios of NF-L:NF-M (c) shows that the filaments dilute like a two-dimensional solid, linear region, at the low weight % NF-M, and the slope is related to the NF diameter. Deviation from linearity corresponds to reaching the two-phase region in the dilution phase diagram (Fig. 4 a).

for the homopolymer (NF-L) and a NF-LM network, at intermediate grafting density of 15 wt% (10 mol %) show that the SAXS data exhibit broad peaks with peak position ( $q_{\text{NF}} = 2\pi/d$ ) shifting to lower  $q$  values as the  $N_G$  networks are diluted to  $N_G$  plus  $I_S$  two-phase at lower protein concentrations with a fixed subunit composition (Fig. 6 a, 0 wt % NF-M and 15 wt % NF-M). In striking contrast, at high NF-M grafting densities (35 wt % NF-M), the SAXS peak position is nearly fixed as more solvent is added.

As with the phase diagrams, the SAXS data for NF-LH gels (Fig. 7 a) is different than with NF-LM gels at higher grafting densities. For low NF-H grafting densities ( $<12.5 \pm 2.5$  wt % NF-H) the SAXS data (Fig. 7 a, 5 wt % and 10 wt % NF-H) shows a broad peak that moves to lower  $q$  as the  $N_G$  phase is diluted from 4.1 wt % protein and the  $N_G$  plus  $I_S$  two-phase is reached at  $\sim 1.6$  wt % protein where a very weak correlation bump of the  $N_G$  phase is still evident (consistent with the phase diagram of Fig. 5 a). For higher NF-H grafting densities (Fig. 7 a, 15 wt % NF-H) upon dilution of the  $N_G$  gel phase, the correlation peak in the SAXS data shifts to lower  $q$  (between 4 wt % and  $\leq 2$  wt % protein) and is seen to be absent at 1.3 wt % protein where the nematic

gel phase undergoes a transition to the isotropic gel plus sol ( $I_G + I_S$ ) two-phase. At even higher NF-H grafting densities (Fig. 7 a, 25 wt % NF-H), a similar trend is observed except that the  $I_G$  plus  $I_S$  two-phase sets in at a higher weight % total protein. The I-N transition occurs between 1.3 wt % and 2 wt % and 2.5–3.1 wt % for 15 wt % and 25 wt % NF-H, respectively. This is in good agreement with values determined using polarized microscopy. The interfilament spacing versus weight % protein at different NF-H grafting densities is summarized in Fig. 7 b. In contrast to the behavior found for the NF-LM network, the interfilament spacing increases with dilution and this trend remains for increasing grafting densities of NF-H. Furthermore, the smallest interfilament spacing observed at high protein concentrations increases from  $\sim 35$  nm for NF-L homopolymer to  $\sim 40$  nm with 70:30 (NF-L/NF-H, wt %) grafting density, which implies that these long protrusions are acting as a spacer preventing close packing of the filaments.

In the  $N_G$  phase, because the dilution of the nematic network by solvent occurs in the plane perpendicular to the filament axis (i.e., in two dimensions), one expects a volume fraction proportionality to the  $d$  spacing of  $d \propto 1/\Phi^{1/2}$  on the



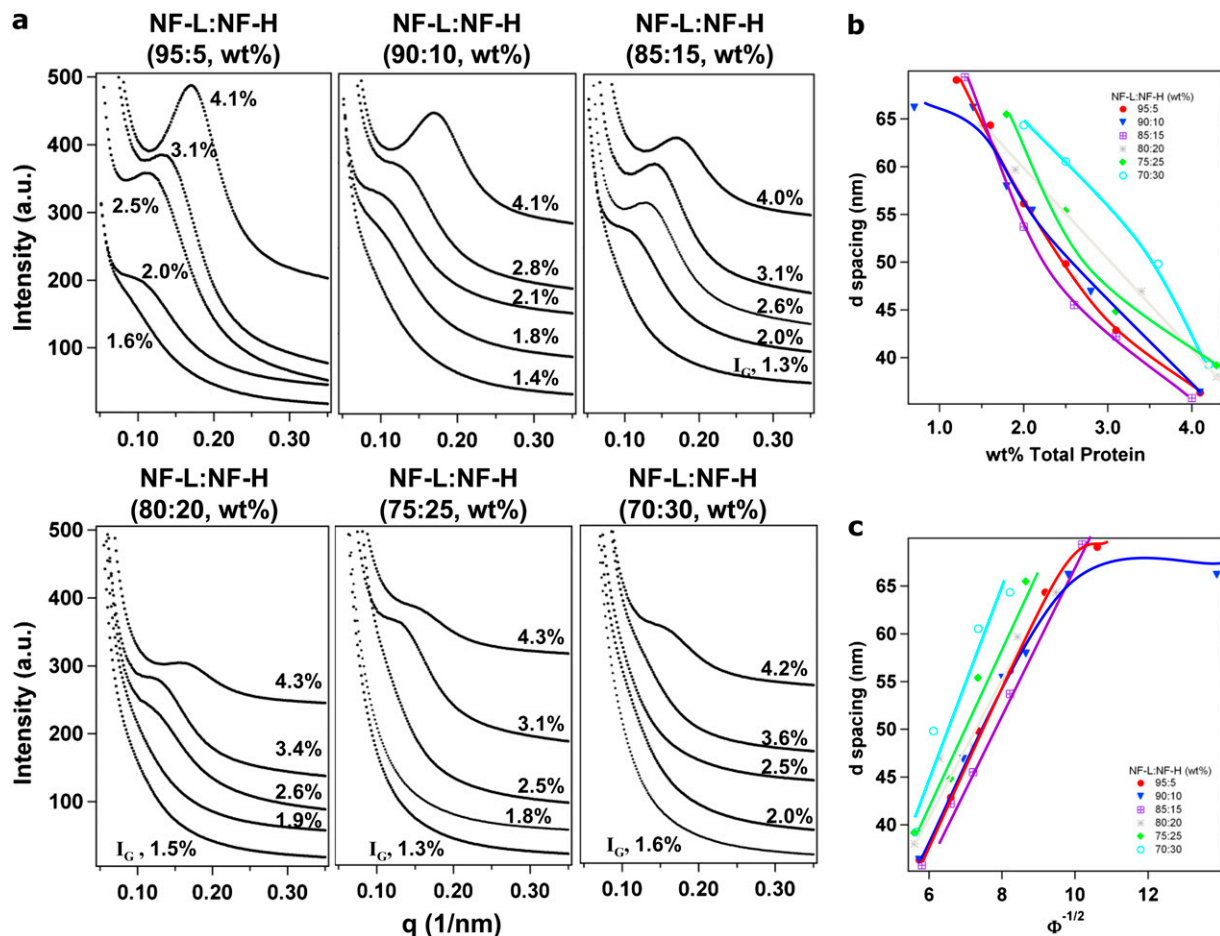


FIGURE 7 Exemplary SAXS scans of dilution series of NF-LH networks (a) for increasing grafting densities of NF-H (86 mM monovalent salt) labeled with weight % total protein (shown on a log-log scale in the Supplementary Material figures, [Data S1](#)). The primary correlation peak becomes much broader at high weight % total protein with increasing NF-H grafting density and disappears when the samples enter the isotropic gel phase ( $I_G$ ) at low weight % total protein. A compilation of the center-to-center interfilament distance ( $d$  spacing) for NF-LH networks as determined with SAXS versus weight % total protein (b) shows that the interfilament spacing increases upon dilution until a correlation peak is no longer detectable when the isotropic phase is reached (as seen in the dilution phase diagram). The linear dependence of the  $d$  spacing versus volume fraction<sup>-1/2</sup> ( $\Phi^{-1/2}$ ) plot for various weight ratios of NF-L/NF-H indicates that the filaments dilute like a two-dimensional solid and the slope is related to the NF diameter.

repulsive side of the interfilament potential (or force) versus  $d$  curve. In all cases, a force was applied to the NF networks during centrifugation, instituting an energetically unfavorable compaction of the gels to a high protein concentration. Repulsive forces dominate during dilution, seen as gel swelling under polarized microscopy, and the interfilament spacing increases. The change in the equilibrium  $d$  spacing with dilution follows a linear trend when plotted against  $\Phi^{-1/2}$  (Figs. 6 c and 7 c). For networks containing NF-L alone, NF-LM, or NF-LH at low weight % NF-H (<15 wt % NF-H), the curves deviate from linearity to a constant  $d$  spacing, indicating equilibrium due to competing attractive and repulsive interfilament forces. This is the stabilized nematic seen in two-phase ( $N_G + I_S$ ) region of the phase diagrams. For NF-LM nematic gels, the equilibrium  $d$  spacing decreases from  $\sim 62$  nm for 0 wt % NF-M to  $\sim 48$  nm for 35 wt % NF-M, showing the increase in filament attraction with NF-M grafting density. The linear behavior shown in Fig. 7 c indicates that

repulsive interactions dominate the NF-LH networks at high weight % NF-H, corresponding to the  $N_G$  phase where the filaments have orientational order.

The closest interfilament spacing observed for the NF-L homopolymer is 38 nm. This means that the short tails are causing a 28 nm spacing between filament cores. The NF sidearms can be thought of as polymer brushes grafted to a cylindrical surface. For the NF-L homopolymer, there are 32 short tails per 45 nm section of a filament. This means that the grafting density is high enough that the tails impinge on the volume occupied by the surrounding chain, assuming a Gaussian chain conformation, and the NF-L tails are in the brush regime. Using the 28 nm spacing between filament cores, this would give a NF-L brush height of 14 nm. With the addition of the longer sidearm subunits, mixed brush theory predicts that the longer chains will be expelled to the periphery of the shorter chains, creating a flower-like conformation (44). Assuming this is the case for NFs, as was explored in a recent

self-consistent field analysis of NF brush height (45,46), and due to the cylindrical grafting surface, if the long chains are pushed to the outside of the 14 nm NF-L brushes, then the long tails have a large volume to explore, which is equivalent to being grafted to a 19 nm diameter cylindrical surface. This could explain the reason that for NF-LM filaments, an increase in filament attraction is not seen until higher grafting densities ( $\geq 20$  wt % NF-M) where the sidearms are more likely to interact with a projection from a neighboring chain.

Assuming that the filaments form a hexagonal lattice, the slope of the linear region of curves in Figs. 6c and 7c is related to the diameter of the filaments ( $r$ ) by the relation  $d/\Phi^{-1/2} = (4\pi/3\sqrt{3})^{1/2}r$ . Extracting the radius of the cores from this equation gives a diameter of  $\sim 8$  nm for NF-LM and 11 nm for the NF-LH networks. The dilution of the NF-LH system is more repulsive over the distances probed by this experiment; therefore the estimate for the core radius is probably more

accurate for these networks. These values closely agree with the accepted 10 nm diameter for intermediate filaments.

The two-component systems have shown that NF-LM forms a more attractive gel than networks composed of NF-LH. This is helpful in understanding the function of the subunits separately, although, in vivo, networks are primarily composed of various ratios of the three components. Fig. 8 is a ternary phase diagram showing the behavior of NF networks with various ratios of the three subunit components. The sides of the diagram represent the two-component systems, the base being the NF-LH and the left side corresponding to the NF-LM, which were previously discussed. Increasing the ratio of NF-H subunits, the networks favor the isotropic gel phase, whereas increasing NF-M leads to the nematic gel phase. The diagram shows that above about a 20 wt % NF-M, the attractive forces within the network are strong enough to align the filaments into a nematic gel. The 7:3:2 subunit composition reported for a bovine spinal cord purification is well into the nematic gel phase and is indicated with a star in the ternary phase diagram.

The most striking difference between the function of the subunit proteins is that NF-M stabilizes the oriented nematic phase whereas NF-H leads to a disordered isotropic phase and the network remains gel-like in both cases. Interestingly, the nematic gel and the isotropic gel can be induced in both systems simply by varying the salt concentration (Fig. 9, a and b). Increasing salt induced nematic ordering in all networks, although the isotropic-nematic (I-N) transition occurs at a higher salt concentration for NF-LH networks. With low salt, the networks are isotropic, although gelation was observed even at the lowest salt concentration probed.

Onsager first suggested that purely repulsive rigid rods acquire nematic ordering at a critical rod volume fraction if the rod length to diameter ratio is greater than 4 (47). The transition is a result of two competing entropic effects, the orientational entropy that favors the isotropic state and the translational entropy that stabilizes the oriented nematic phase at high rod concentrations. The theory was later modified to include semiflexible rods by incorporating the persistence length ( $L_P$ ), a measure of the rigidity of the rod (48,49). This resulted in an isotropic to nematic transition around  $\Phi_{IN} = 5.1D/L_P$ , where  $D$  is the diameter of the rod. For NFs, the predicted transition using an  $L_P$  of  $1 \mu\text{m}$  and the core diameter of 10 nm gives a calculated volume fraction transition of  $\Phi_{IN} = 0.051$ . This is significantly larger than the  $\Phi_{IN} = 0.011$  experimentally observed for the I-N transition for NF-LH networks. This difference can be explained by accounting for the excluded volume effect of the negatively charged sidearms of the filaments. This creates an effective diameter that is much larger than the core of the filaments, analogous to the excluded volume effect due to electrostatic repulsion that was predicted (50) and experimentally shown (51) to significantly decrease the I-N transition. Onsager further predicted that an increase in ionic strength will screen the electrostatic repulsion of charged rods revealing the hard

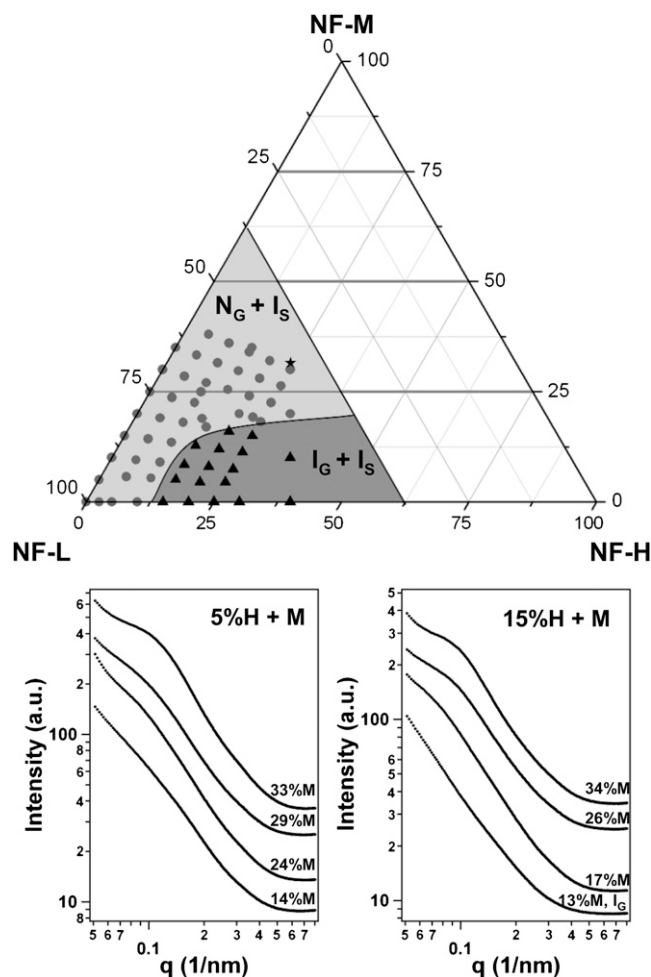


FIGURE 8 Ternary phase diagram showing the phase behavior of filaments composed of all three NF subunits at 86 mM monovalent salt and pH 6.8 in excess buffer. The aligned nematic phase ( $N_G + I_S$ ) is stabilized with increasing weight % NF-M whereas the isotropic gel phase ( $I_G + I_S$ ) occurs with higher weight % NF-H. Small angle synchrotron x-ray diffraction scans show the onset of a correlation peak with increasing weight % NF-M coinciding with nematic ordering.

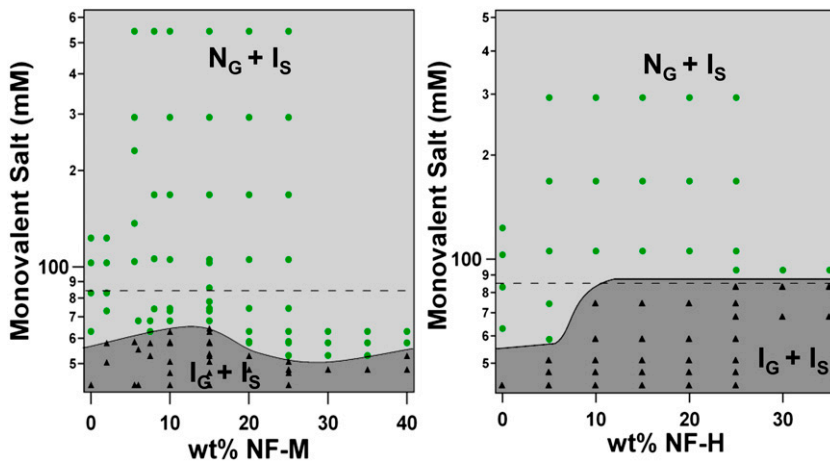


FIGURE 9 NF-LM and NF-LH phase behavior as a function of monovalent salt in excess solvent. The y axis refers to total ionic strength comprised of 43 mM monovalent ions from the MES buffer plus added KCl. The isotropic phase is induced in all compositions at low monovalent salt concentration, and nematic ordering occurs with increasing ionic strength. A higher electrolyte concentration is needed to stabilize the nematic phase with high grafting densities of NF-H, whereas nematic anisotropy appears at low salt concentrations, well below physiological monovalent salt conditions, for NF-LM networks. Dashed lines are at 86 mM monovalent salt and solid lines are guides for the eyes.

rod diameter. This favors the isotropic phase and has the effect of increasing the I-N volume fraction transition. This is opposite of the behavior seen in the NF networks, where increasing salt stabilizes the nematic phase.

The Onsager theory was developed for bare rods and therefore neglects the effect of ionic strength on brush height and possible attractions between interpenetrating sidearms. NF sidearms are polyampholytes, but the fraction of positively and negatively charged groups varies among sidearms as summarized in Table 1. NF-L has the lowest fraction of charged to neutral amino acids but, of the charged amino acids, 78% of them are negatively charged, giving it a higher linear charge density along the sidearm than NF-M. All three sidearms exhibit charge asymmetry, being anionic, but variations in charge distribution and chain length, as seen in Fig. 2, may explain the increased attraction experimentally observed in NF-LM networks. Monte Carlo simulations of spherical colloids with end-grafted polyampholyte diblock copolymers (one anionic, the other cationic) have shown, without added salt, that charge neutrality between blocks leads to colloidal flocculation and interpenetration of brushes (52). Although the NF sidearms have a net negative charge, and thus are repulsive at large interfilament spacings, the screening effect of the salt will allow local interactions (e.g., salt bridges and hydrogen bonds) among sidearms causing filament attraction, at small interfilament spacings, and stabilization of the nematic phase. As seen experimentally, this attraction exists for NF-L and NF-LH networks but at a higher monovalent salt concentration than for NF-LM. It is clear from this work that sidearm attraction can occur between both NF-M and NF-H sidearms in the appropriate solvent conditions and without the help of accessory proteins.

## CONCLUSION

The interactions among NFs are expected to be highly dependent on the ratio of the three subunits comprising the filaments, their precise phosphorylation states, and solvent conditions (ionic strength and pH). The interfilament spacing

can be related to interactions among assembled neurofilaments, and we show that SAXS is a good probe of this distance. Near physiological salt conditions, NF-LM networks align to form a nematic gel, whereas NF-LH favors a more expansive isotropic gel. This suggests that repulsive interactions dominate among filaments composed of NF-LH. For NF-LM networks, attractive forces tend to align the filaments whereas steric repulsion results in an interfilament spacing significantly larger than the 10 nm filament core.

These interactions can be tailored by subtle changes in monovalent salt concentration. For all filament subunit compositions, low ionic strength results in a repulsive isotropic gel, whereas increasing salt induces nematic ordering and a decrease in interfilament spacing. The transition between the isotropic and the nematic phase is within the range of the cation concentration of neurons, suggesting that small changes in the salt environment will affect the NF scaffold within cells, making it more compact and potentially less ideal for axonal transport. Competing attractive and repulsive forces observed may be a natural mechanism for maintaining an aligned yet spacious network.

This work raises questions about the state of the NFs within the neuronal cell body and axon. Variations in filament composition exist throughout development and even within various regions of a neuron. Presumably, *in vivo* filaments are composed of a combination of the three subunit proteins. The well known 7:3:2 (NF-L/NF-M/NF-H) subunit ratio was found to be a nematic gel, although less tightly bundled than NF-LM networks supporting the typical imaged of aligned filaments within axons (5). During nerve regeneration, filaments are mainly composed of NF-LM (25), which would also be in the nematic phase. From reported NF compositions *in vivo*, it seems that the nematic phase dominates, although, as this work shows, changes in NF composition could lead to significant structural changes in the cytoskeleton.

## SUPPLEMENTARY MATERIAL

To view all of the supplemental files associated with this article, visit [www.biophysj.org](http://www.biophysj.org).

We thank Abby Oehler and Tracy MacDonough for assistance with the grafting density experiments and Miguel Ojeda Lopez for his aid in the crude NF purification. We are also grateful for many useful discussions with Herb Miller, Phil Pincus, Joanna Deek, and Roy Beck.

This work is supported by Department of Energy grant DE-FG02-06ER46314 and National Science Foundation grants DMR-0503347 and DMR-0803103. The Stanford Synchrotron Radiation Laboratory, where the x-ray scattering work was performed, is supported by the U.S. Department of Energy.

## REFERENCES

- Cohlberg, J. A., H. Hajarian, T. Tran, P. Alipourjehdi, and A. Noveen. 1995. Neurofilament protein heterotetramers as assembly intermediates. *J. Biol. Chem.* 270:9334–9339.
- Ching, G., and R. Liem. 1993. Assembly of type IV neuronal intermediate filaments in nonneuronal cells in the absence of preexisting cytoplasmic intermediate filaments. *J. Cell Biol.* 122:1323–1335.
- Geisler, N., and K. Weber. 1981. Self-assembly in vitro of the 68,000 molecular weight component of the mammalian neurofilament triplet proteins into intermediate-sized filaments. *J. Mol. Biol.* 151:565–571.
- Fuchs, E., and D. W. Cleveland. 1998. A structural scaffolding of intermediate filaments in health and disease. *Science.* 279:514–519.
- Hirokawa, N., M. A. Glicksman, and M. B. Willard. 1984. Organization of mammalian neurofilament polypeptides within the neuronal cytoskeleton. *J. Cell Biol.* 98:1523–1536.
- Leterrier, J. F., J. Kas, J. Hartwig, R. Vegners, and P. A. Janmey. 1996. Mechanical effects of neurofilament cross-bridges—modulation by phosphorylation, lipids, and interactions with F-actin. *J. Biol. Chem.* 271:15687–15694.
- Chen, J. G., T. Nakata, Z. Z. Zhang, and N. Hirokawa. 2000. The C-terminal tail domain of neurofilament protein-H (NF-H) forms the crossbridges and regulates neurofilament bundle formation. *J. Cell Sci.* 113:3861–3869.
- Kumar, S., X. Yin, B. D. Trapp, J. H. Hoh, and M. E. Paulaitis. 2002. Relating interactions between neurofilaments to the structure of axonal neurofilament distributions through polymer brush models. *Biophys. J.* 82:2360–2372.
- Brown, H. G., and J. H. Hoh. 1997. Entropic exclusion by neurofilament sidearms: a mechanism for maintaining interfilament spacing. *Biochemistry.* 36:15035–15040.
- Guo, Y.-T., Y.-M. Li, Z.-T. Zhu, and Y.-F. Zhao. 2005. Effect of the phosphate group with different negative charges on the conformation of phosphorylated Ser/Thr-Pro Motif. *Int. J. Pept. Res. Ther.* 11:159–165.
- Trimpin, S., A. E. Mixon, M. D. Stapels, M.-Y. Kim, P. S. Spencer, and M. L. Deinzer. 2004. Identification of endogenous phosphorylation sites of bovine medium and low molecular weight neurofilament proteins by tandem mass spectrometry. *Biochemistry.* 43:2091–2105.
- Jones, S., and R. Williams, Jr. 1982. Phosphate content of mammalian neurofilaments. *J. Biol. Chem.* 257:9902–9905.
- Nixon, R., S. Lewis, and C. Marotta. 1987. Posttranslational modification of neurofilament proteins by phosphate during axoplasmic transport in retinal ganglion cell neurons. *J. Neurosci.* 7:1145–1158.
- Barrat, J.-L., and J.-F. Joanny. 1997. *Theory of Polyelectrolyte Solutions.* Wiley.
- Rühe, J., M. Ballauff, M. Biesalski, P. Dziezok, F. Gröhn, D. Johannsmann, N. Houbenov, N. Hugenberg, R. Konradi, S. Minko, M. Motornov, R. R. Netz, M. Schmidt, C. Seidel, M. Stamm, T. Stephan, D. Usov, and H. Zhang. 2004. Polyelectrolyte brushes. In *Polyelectrolytes with Defined Molecular Architecture I*. 79–150.
- Ballauff, M., and O. Borisov. 2006. Polyelectrolyte brushes. *Curr. Opin. Colloid Interface Sci.* 11:316–323.
- Dobrynin, A. V., and M. Rubinstein. 2005. Theory of polyelectrolytes in solutions and at surfaces. *Prog. Polym. Sci.* 30:1049–1118.
- Shaw, G. 1998. *Neurofilaments.* Springer, Berlin.
- Hisanaga, S.-i., and N. Hirokawa. 1988. Structure of the peripheral domains of neurofilaments revealed by low angle rotary shadowing. *J. Mol. Biol.* 202:297–305.
- Liu, J., X. Tong, S. Pang, and Z. Zhai. 1999. The periodicity in the structure of native neurofilaments studied with scanning tunneling microscopy. *Appl. Surf. Sci.* 144–145:644–647.
- Xu, Z., J. R. Marszalek, M. K. Lee, P. C. Wong, J. Folmer, T. O. Crawford, S. T. Hsieh, J. W. Griffin, and D. W. Cleveland. 1996. Subunit composition of neurofilaments specifies axonal diameter. *J. Cell Biol.* 133:1061–1069.
- Carden, M., J. Trojanowski, W. Schlaepfer, and V. Lee. 1987. Two-stage expression of neurofilament polypeptides during rat neurogenesis with early establishment of adult phosphorylation patterns. *J. Neurosci.* 7:3489–3504.
- Shaw, G., and K. Weber. 1982. Differential expression of neurofilament triplet proteins in brain development. *Nature.* 298:277–279.
- Drake, P., and R. Lasek. 1984. Regional differences in the neuronal cytoskeleton. *J. Neurosci.* 4:1173–1186.
- Tsuda, M., T. Tashiro, and Y. Komiya. 2000. Selective solubilization of high-molecular-mass neurofilament subunit during nerve regeneration. *J. Neurochem.* 74:860–868.
- Xu, Z., L. C. Cork, J. W. Griffin, and D. W. Cleveland. 1993. Increased expression of neurofilament subunit NF-L produces morphological alterations that resemble the pathology of human motor neuron disease. *Cell.* 73:23–33.
- Wong, P. C., J. Marszalek, T. O. Crawford, Z. Xu, S. T. Hsieh, J. W. Griffin, and D. W. Cleveland. 1995. Increasing neurofilament subunit NF-M expression reduces axonal NF-H, inhibits radial growth, and results in neurofilamentous accumulation in motor neurons. *J. Cell Biol.* 130:1413–1422.
- Watson, D. F., F. N. Nachtman, R. W. Kuncel, and J. W. Griffin. 1994. Altered neurofilament phosphorylation and beta tubulin isoforms in Charcot-Marie-Tooth disease type 1. *Neurology.* 44:2383–2387.
- Hirano, A., H. Donnenfeld, S. Sasaki, and I. Nakano. 1984. Fine structural observations of neurofilamentous changes in amyotrophic lateral sclerosis. *J. Neuropathol. Exp. Neurol.* 43:461–470.
- Schmidt, M. L., J. A. Martin, V. M. Lee, and J. Q. Trojanowski. 1996. Convergence of Lewy bodies and neurofibrillary tangles in amygdala neurons of Alzheimer's disease and Lewy body disorders. *Acta Neuropathol. (Berl.).* 91:475–481.
- Julien, J. P., F. Cote, and J. F. Collard. 1995. Mice overexpressing the human neurofilament heavy gene as a model of ALS. *Neurobiol. Aging.* 16:487–490.
- Leterrier, J. F., and J. Eyer. 1987. Properties of highly viscous gels formed by neurofilaments in vitro. A possible consequence of a specific inter-filament cross-bridging. *Biochem. J.* 245:93–101.
- Liem, R. K. 1986. Purification of neurofilaments and their constituent polypeptides. *Methods Enzymol.* 134:380–388.
- Hammersley, A. P. 1997. FIT2D: An Introduction and Overview. ESRF Internal Report ESRF97HA02T.
- Hammersley, A. P., S. O. Svensson, M. Hanfland, A. N. Fitch, and D. Häusermann. 1996. Two-dimensional detector software: from real detector to idealised image or two-theta scan. *High Pressure Res.* 14:235–248.
- Herrmann, H., and U. Aebi. 2004. Intermediate filaments: molecular structure, assembly mechanism, and integration into functionally distinct intracellular Scaffolds. *Annu. Rev. Biochem.* 73:749–789.
- Herrmann, H., M. Haner, M. Brettel, N. O. Ku, and U. Aebi. 1999. Characterization of distinct early assembly units of different intermediate filament proteins. *J. Mol. Biol.* 286:1403–1420.
- Hisanaga, S., A. Ikai, and N. Hirokawa. 1990. Molecular architecture of the neurofilament. 1. Subunit arrangement of neurofilament-L

- protein in the intermediate-sized filament. *J. Mol. Biol.* 211:857–869.
39. Hisanaga, S., and N. Hirokawa. 1990. Molecular architecture of the neurofilament. 2. Reassembly process of neurofilament-L protein in vitro. *J. Mol. Biol.* 211:871–882.
  40. Lubensky, T. C., R. Mukhopadhyay, L. Radzihovsky, and X. Xing. 2002. Symmetries and elasticity of nematic gels. *Phys. Rev. E.* 66: 011702.
  41. Nelson, D. R., and H. S. Seung. 1989. Theory of melted flux liquids. *Phys. Rev. B.* 39:9153.
  42. Selinger, J. V., and R. F. Bruinsma. 1991. Hexagonal and nematic phases of chains. I. Correlation functions. *Phys. Rev. A.* 43:2910.
  43. Selinger, J. V., and R. F. Bruinsma. 1991. Hexagonal and nematic phases of chains. II. Phase transitions. *Phys. Rev. A.* 43:2922.
  44. Skvortsov, A. M., L. I. Klushin, and A. A. Gorbunov. 1997. Long and short chains in a polymeric brush: a conformational transition. *Macromolecules.* 30:1818–1827.
  45. Zhulina, E. B., and F. A. M. Leermakers. 2007. A self-consistent field analysis of the neurofilament brush with amino-acid resolution. *Biophys. J.* 93:1421–1430.
  46. Zhulina, E. B., and F. A. M. Leermakers. 2007. Effect of the ionic strength and pH on the equilibrium structure of a neurofilament brush. *Biophys. J.* 93:1452–1463.
  47. Onsager, L. 1949. The effects of shape on the interaction of colloidal particles. *Ann. N.Y. Acad. Sci.* 51:627–659.
  48. Khokhlov, A. R., and A. N. Semenov. 1981. Liquid-crystalline ordering in the solution of long persistent chains. *Physica A.* 108: 546–556.
  49. Vroege, G. J., and H. N. W. Lekkerkerker. 1992. Phase transitions in lyotropic colloidal and polymer liquid crystals. *Rep. Prog. Phys.* 55: 1241–1309.
  50. Stroobants, A., H. N. W. Lekkerkerker, and T. Odijk. 1986. Effect of electrostatic interaction on the liquid crystal phase transition in solutions of rodlike polyelectrolytes. *Macromolecules.* 19:2232–2238.
  51. Fraden, S., G. Maret, D. L. D. Caspar, and R. B. Meyer. 1989. Isotropic-nematic phase transition and angular correlations in isotropic suspensions of tobacco mosaic virus. *Phys. Rev. Lett.* 63:2068–2071.
  52. Linse, P. 2007. Interaction between colloids with grafted diblock polyampholytes. *J. Chem. Phys.* 126:114903–114913.